

Article

Influences of Zr and V Addition on the Crystal Chemistry of θ -Al₁₃Fe₄ and the Grain Refinement of α -Al in an Al-4Fe Alloy Based on Experiment and First-Principle Calculations

Zhongping Que ^{*}, Changming Fang , Junhai Xia and Zhongyun Fan 

Brunel Centre of Advanced Solidification Technology (BCAST), Brunel University London, Uxbridge UB8 3PH, UK; Changming.Fang@brunel.ac.uk (C.F.); junhai.xia@hotmail.com (J.X.); Zhongyun.Fan@brunel.ac.uk (Z.F.)

* Correspondence: Zhongping.Que@brunel.ac.uk; Tel.: +44-1895-268535

Abstract: Fe-containing intermetallic compounds (IMCs) are among the most detrimental second phases in aluminum alloys. One particularly harmful type is θ -Al₁₃Fe₄, which exhibits a needle- or plate-like morphology, leading to greater degradation of mechanical properties compared to other Fe-IMCs with more compact structures, such as α -Al₁₅(Fe,Mn)₃Si₂. The addition of alloying elements is a crucial strategy for modifying the microstructure during the solidification process of aluminum alloys. This study investigates the effects of adding vanadium (V) and zirconium (Zr) on the morphology and crystal chemistry of θ -Al₁₃Fe₄ in an Al-4Fe alloy, employing a combination of experimental observations, first-principle calculations, and thermodynamic analysis. Our findings indicate that zirconium significantly refines both the primary θ -Al₁₃Fe₄ particles and the α -Al grains. Additionally, a small amount of vanadium can be incorporated into one of the Wyckoff 4i Al sites in θ -Al₁₃Fe₄, rather than occupying any Fe sites, under casting conditions, in addition to the formation of binary Al-V phases.

Keywords: θ -Al₁₃Fe₄; Zr; V; Al-4Fe alloy; first-principle calculations



Citation: Que, Z.; Fang, C.; Xia, J.; Fan, Z. Influences of Zr and V Addition on the Crystal Chemistry of θ -Al₁₃Fe₄ and the Grain Refinement of α -Al in an Al-4Fe Alloy Based on Experiment and First-Principle Calculations. *Crystals* **2024**, *14*, 879. <https://doi.org/10.3390/cryst14100879>

Academic Editor: Benilde F. O. Costa

Received: 1 September 2024

Revised: 2 October 2024

Accepted: 7 October 2024

Published: 9 October 2024



Copyright: © 2024 by the authors. Licensee MDPI, Basel, Switzerland. This article is an open access article distributed under the terms and conditions of the Creative Commons Attribution (CC BY) license (<https://creativecommons.org/licenses/by/4.0/>).

1. Introduction

Fe-containing intermetallic compounds (Fe-IMCs) usually form as coarse particles with complex morphologies in aluminum alloys during casting [1]. Fe-IMCs especially those with needle-like or plate-like morphologies such as θ -Al₁₃Fe₄ have detrimental effects on the ductility of the cast Al alloys. The issue becomes more pronounced in recycled aluminum alloys, where iron content can accumulate over multiple recycling cycles. Several approaches have been explored in recent decades to address iron accumulation in aluminum alloys [2–7]. One developed method is the de-iron treatment, which leverages the density differences between iron intermetallic compounds and the aluminum melt to promote sedimentation of primary Fe compounds [6]. A desirable de-ironing effect can be achieved by applying the intensive shearing technology [7]. Other treatment paths such as ultrasonic processing [8] and super heating have been used to reduce the Fe concentration in the melt through formation of primary Fe intermetallic compounds [9,10]. Modification of the Fe-IMCs is also one of the approaches by introducing minor alloying element addition, which can alter their morphologies. [11,12].

Fe-IMCs generally have complex crystal structures and chemical compositions compared to α -Al, making them more challenging to nucleate heterogeneously [13]. The formation of Fe-IMCs is also very sensitive to the formation conditions such as alloy composition and cooling rate [1]. For example, θ -Al₁₃Fe₄ exhibits a diverse range of crystal chemistry. It contains 20 crystallographically different types of atoms (5 Fe and 15 Al species), highlighting its flexibility to accommodate alloying elements [1]. Therefore, the morphology and crystal chemistry of θ -Al₁₃Fe₄ particles can be manipulated by doping

with alloying elements. Previous studies have shown that the 3d transition metals such as Mn, Cr, Co, Ni, Cu, etc. can be doped individually or in combination at the Fe sites in θ -Al₁₃Fe₄, resulting in corresponding modifications to the lattice parameters and morphology of the θ -Al₁₃Fe₄ [14–17]. Meanwhile, the doping of the other alloying elements, such as V and Zr in this Fe-IMC, has been rarely reported.

Vanadium is a 3d element located as a relatively distant neighbor of iron in the Periodic Table. It has a smaller atomic radius of 179 pm compared to that of Fe, which is 194 pm. Al₃V particles formed during casting may serve as potential nucleation substrates for α -Al [17]. To date, there are no reports on vanadium solubility in θ -Al₁₃Fe₄. Zirconium is a 4d element and has an atomic radius of 186 pm. Zr is commonly considered to be a favorable element for the grain refinement of Al alloy [17,18]. Furthermore, due to the peritectic nature of the binary Al-Zr phase diagram, adding zirconium at concentrations higher than 0.11 wt.% can effectively refine α -Al grains by forming Al₃Zr (D023) in the melt [18]. Although there are reports about the impacts of Zr addition on improvement of the microstructure and properties of Al-Fe alloys [19–22], the understanding of the effects of Zr on the crystal chemical of θ -Al₁₃Fe₄ is still limited. In this study, we investigated the comprehensive effects of V and Zr additions on the modification and refinement of θ -Al₁₃Fe₄ particles, as well as on the grain refinement of α -Al, using a combined approach of experimental observations, first-principle calculations and thermodynamic analysis. Al-5Ti-1B grain refiner is one of the most effective grain refiners for aluminum alloys. Therefore, the grain refinement of α -Al achieved through the addition of Zr in this study was compared to that obtained with the commercial Al-5Ti-1B grain refiner. Our study revealed that doping with both vanadium and zirconium at the Fe sites in θ -Al₁₃Fe₄ incurs high energy costs. However, a small amount of vanadium can be doped into one of the Wyckoff 4i Al sites in θ -Al₁₃Fe₄ at the casting temperature.

2. Experimental

2.1. Casting and Characterization

A binary Al-4Fe alloy (all compositions are in wt.%, unless otherwise stated) was prepared by melting purity Al (>99.99%) and Al-45Fe master alloy in an electric resistance furnace. The pure Al was molten at 900 °C followed by the addition of Al-45Fe master alloy. Sufficient stirring was applied until the Al-45Fe master alloy fully dissolved, ensuring the chemical homogeneity of the melt. The prepared melt was separated into equal amount variety additions. To investigate the effects of zirconium addition on microstructural changes, varying amounts of zirconium (0, 0.1, 0.2, 0.3, 0.4, 0.5, 0.6, and 1.0%) were introduced using an Al-10Zr master alloy into the prepared Al-4Fe alloy. To assess microstructural variations, 0, 0.1, and 0.5% of vanadium were added to the Al-4Fe alloy using an Al-10V master alloy. Additionally, to compare the effects of zirconium and vanadium additions on the grain refinement of Al-4Fe, the commercial Al-5Ti-1B grain refiner was also added to the alloy as a reference for the grain refinement of α -Al.

The Al-Fe melts, both with and without different additions, were cast at a pouring temperature of 800 °C into a Tp-1 mold, which was immediately cooled using a water spray with a controlled flow rate of 3.8 L/min [23]. A specific cooling rate of 3.5 K/s, similar to that of the directional casting, was achievable in Tp-1 mold at a sample section located 38 mm from the bottom. Tp-1 mold was pre-heated at a standard temperature of 380 °C. A steel mold with a mushroom shape, designed for composition measurement purpose, was casted following Tp-1 casting for each melt. A sample consisting of a 1 cm-thick flat round plate with a handlebar in the middle can be cast from the mushroom mold. The rest of the melts were kept in the furnace and naturally cooled down to 200 °C. The average cooling rate, calculated based on the temperature difference (200–800 °C) and the cooling time, is 0.02 K/s in this study. The composition of studied alloys was measured using a foundry master alloy with stationary optical emission spectrometers, as shown in Table 1. The phase diagram and the solidification curve of Al-4Fe-0.5Zr and Al-4Fe-0.5V alloys were

calculated using Pandat software with the PanAluminum 2020 database [24], employing the Scheil solidification model [25].

Table 1. Measured composition of studied alloys.

Alloys	Alloying Elements wt.%										
	Fe	Zr	V	Mn	Cr	Ni	Ti	Cu	Zn	Si	Mo
Al-4.0Fe	4.18	-	-	0.01	0.01	0.01	-	-	0.01	-	0.01
Al-4Fe-0.5Zr	3.86	0.57	0.01	0.01	0.01	0.02	-	-	0.01	-	
Al-4.0Fe-0.1V	3.73	-	0.10	0.01	0.01	0.02	0.01	-	0.01	-	0.01
Al-4.0Fe-0.5V	3.85	-	0.52	0.02	0.02	0.01	0.01	0.01	0.02	0.04	0.01

Note: - in the table means non-detectable.

Metallurgical investigations were conducted on the cross section taken at a height of 38 mm from the bottom of the Tp-1 sample, which exhibited a specific cooling rate of 3.5 K/s [24]. Optical and scanning electron microscopes (SEM) were used for microstructure characterization. A Zeiss Leo SEM, equipped with EDX spectroscopy, was operated at an accelerating voltage of 15–20 kV. The α -Al grains were observed and quantified using an anodizing technique, which involved etching the aluminum sample in Barker's reagent (a diluted fluoroboric acid solution). The average grain size of α -Al was estimated using the linear intercept method described in ASTM standard E112. The size and number density of the primary θ -Al₁₃Fe₄ particles were also quantified. Due to the challenges in measuring the needle-like θ -Al₁₃Fe₄, the assessment was based on the cross section of the θ -Al₁₃Fe₄ needles. To observe the 3-dimensional (3D) morphology of intermetallic compounds in this study, the as-cast samples were deep etched in 15% HCl solution for 2–3 min followed by the methanol bath. X-ray diffraction (XRD) studies were used to identify the phases using a Bruker D500 (Cu K α) operating at 40 kV and 40 mA.

2.2. First-Principle Calculations

The first-principle Vienna Ab initio Simulation Package (VASP) [26] was utilized in this study. This code employs the density functional theory (DFT) within the projector-augmented wave approach [27]. The Generalized Gradient Approximation (GGA-PBE) [27] was applied for the exchange and correlation energy terms because the GGA functions better for the *d* metals such as vanadium, iron, zirconium and related compounds than the Local Density Approximation [28,29]. The cut-off energy of the wave functions was set to 550 eV and the cut-off energy of the augmentation functions to 700 eV (1 eV is equal to 1.6022×10^{-19} J). These values are higher than the corresponding default values. The electronic wave functions were sampled with a $4 \times 8 \times 6$ grid (70 to 100 k-points) in the irreducible Brillouin zone (BZ) of θ -Al₁₃Fe₄ and the related compositions depending on the symmetry, using the Monkhorst–Pack method [30]. First-principle structural optimizations were performed for both lattice parameters and the coordinates of the atoms. Different *k*-meshes and cut-off energies were used for the wave functions and augmentation wave functions, respectively. Tests showed good convergence with deviation within 1 meV per atom.

3. Results

3.1. The Effects of Zr on the Refinement of θ -Al₁₃Fe₄

Figure 1 shows the as-cast microstructure of Al-4Fe alloys with and without 0.5% Zr solidified at 3.5 K/s. Figure 1a shows the primary θ -Al₁₃Fe₄ particles with a star-like morphology in the Al-4Fe alloy. In Al-4Fe alloy, the primary θ phase can be observed with up to ten-fold symmetry. The size of primary θ -Al₁₃Fe₄ particles, measured along the cross section of the needles, was found to be $120.3 \pm 13.2 \mu\text{m}$, as shown in Table 2. The number density was measured as $27.6 \pm 6.7 \text{ mm}^{-2}$. Figure 1b shows the obviously refined primary θ -Al₁₃Fe₄ particles in Al-4Fe-0.5Zr alloy. The average measured size of primary θ -Al₁₃Fe₄ particles was $22.5 \pm 0.9 \mu\text{m}$. The number density of these IMCs was significantly increased to $194.4 \pm 32.5 \text{ mm}^{-2}$.

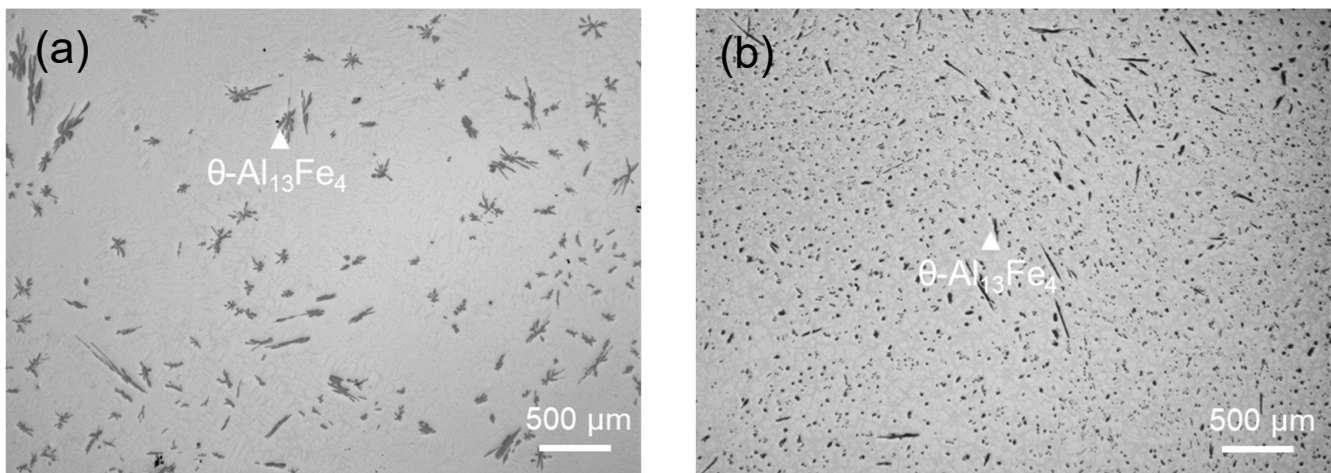


Figure 1. Optical microscope (OM) image demonstrating that the 0.5 wt.% Zr addition refined the primary θ - $\text{Al}_{13}\text{Fe}_4$ in Al-4Fe alloy solidified at 3.5 K/s. (a) The primary θ - $\text{Al}_{13}\text{Fe}_4$ with star-like morphology in Al-4Fe alloy, and (b) the refined primary θ - $\text{Al}_{13}\text{Fe}_4$ in Al-4Fe-0.5Zr alloy.

Table 2. The effects of Zr and V on the θ - $\text{Al}_{13}\text{Fe}_4$ and grain size in studied alloys.

Alloy (wt.%)	θ - $\text{Al}_{13}\text{Fe}_4$ (Branches)		α -Al
	Section Size (μm)	Number Density (mm^{-2})	Grain Size
Al-4.0Fe	120.3 ± 13.2	27.6 ± 6.7	435.2 ± 40.8
Al-4.0Fe (Al-5Ti-1B)	-	-	$153 \pm 3.1 \mu\text{m}$
Al-4Fe-0.5Zr	22.5 ± 0.9	194.4 ± 32.5	63.1 ± 2.8
Al-4.0Fe-0.1V	92.2 ± 13.8	Only a few can be seen	-
Al-4.0Fe-0.5V	119.9 ± 20	Only a few can be seen	921.3 ± 50.4

Note: - in the table means non-detectable.

Figure 2 shows the further SEM investigation on the microstructure of Al-4Fe with and without 0.5% Zr addition and solidified at 3.5 K/s. Figure 2a illustrates that the primary θ - $\text{Al}_{13}\text{Fe}_4$ particles in the Al-4Fe alloy are large, with most exhibiting ten-fold branches. The θ - $\text{Al}_{13}\text{Fe}_4$ particles in binary eutectic have a needle-/plate-like morphology and large size compared to that in Al-4Fe-0.5Zr (Figure 2b). Figure 2b shows multiple primary intermetallic compounds solidified in Al-4Fe-0.5Zr alloy at 3.5 K/s. They are the refined θ - $\text{Al}_{13}\text{Fe}_4$ particles, along with some Zr-rich particles exhibiting cubic or needle-like morphologies, with refined binary eutectic (θ - $\text{Al}_{13}\text{Fe}_4$ + α -Al). The morphology of primary θ - $\text{Al}_{13}\text{Fe}_4$ particles in Al-4Fe-0.5Zr alloy is slightly different to that in Al-4Fe alloy. The primary θ - $\text{Al}_{13}\text{Fe}_4$ particles have a larger size in Al-4Fe-0.5Zr alloy and normally have ten-fold symmetry, which is same as that in Al-4Fe alloy. However, some primary θ - $\text{Al}_{13}\text{Fe}_4$ particles have a small size ($<25 \mu\text{m}$) and only have two branches or no branch viewed from the cross section. The SEM-EDS results presented in Table 3 indicate that the no Zr can be detected in the θ - $\text{Al}_{13}\text{Fe}_4$ phase, and no Fe is present in the Zr-rich compounds. The Zr-rich IMCs with cubic morphology are the major Zr-IMCs which was identified as the equilibrium Al_3Zr DO₂₃, confirmed through SEM-EDS and XRD analyses. Various non-equilibrium zirconium-rich intermetallic compounds (IMCs) with different morphologies, such as needle-like structures (Figure 2b), can also be observed in the Al-4Fe-0.5Zr alloy solidified at the high cooling rate of 3.5 K/s. More importantly, the binary eutectic (θ - $\text{Al}_{13}\text{Fe}_4$ + α -Al) in the Al-4Fe-0.5Zr alloy was obviously refined compared to that in Al-4Fe alloy.

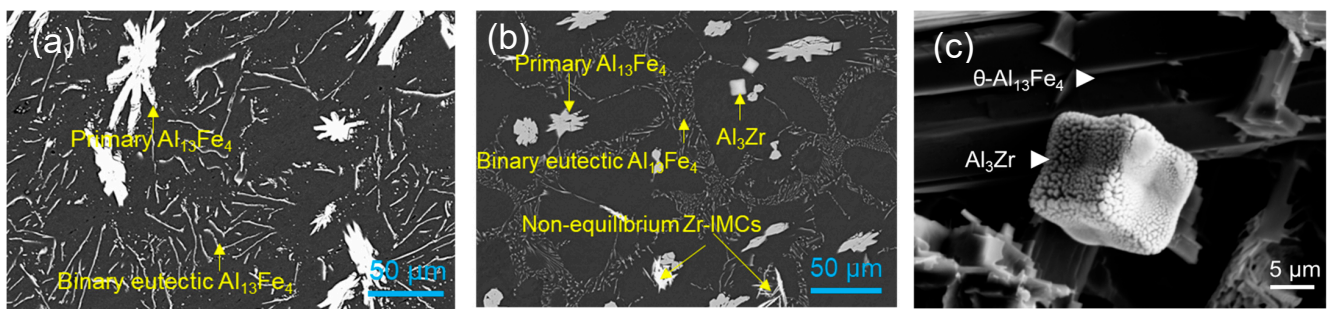


Figure 2. The scanning electron microscopy (SEM) images showing (a) the star-like primary θ - $\text{Al}_{13}\text{Fe}_4$ particles and coarse needle-/plate-like θ - $\text{Al}_{13}\text{Fe}_4$ in binary eutectic (θ - $\text{Al}_{13}\text{Fe}_4 + \alpha$ -Al) in Al-4Fe alloy, (b) the refined primary θ - $\text{Al}_{13}\text{Fe}_4$ particles and some Zr-rich particles with cubic or needle-like morphologies with refined binary eutectic (θ - $\text{Al}_{13}\text{Fe}_4 + \alpha$ -Al) in Al-4Fe-0.5Zr alloy, and (c) 3-dimensional (3D) morphology of the primary Al_3Zr attached with the primary θ - $\text{Al}_{13}\text{Fe}_4$ in Al-4Fe-0.5Zr alloy.

Table 3. The SEM-EDS of different types of intermetallic compounds in studied alloys.

Alloys	Primary IMCs	Average Composition (at.%)					Formula Related to Composition
		Al	Fe	V	Fe + V	Zr	
Al-4Fe	$\text{Al}_{13}\text{Fe}_4$ (only)	74.75 ± 0.05	25.25 ± 0.01	-	-	-	$\text{Al}_{13}\text{Fe}_4$
Al-4Fe-0.5Zr	$\text{Al}_{13}\text{Fe}_4$ (dominated)	75.14 ± 0.04	24.86 ± 0.01	-	-	-	$\text{Al}_{13}\text{Fe}_4$
Al-4Fe-0.1V	$\text{Al}_{13}\text{Fe}_4$ (major, brighter)	77.92 ± 0.05	21.91 ± 0.02	0.16 ± 0.01	22.07	-	$\text{Al}_{13}\text{Fe}_4$
Al-4Fe-0.1V	$\text{Al}_{13}\text{Fe}_4$ (major, brighter)	77.87 ± 0.05	21.79 ± 0.02	0.35 ± 0.01	22.14	-	$\text{Al}_{13}\text{Fe}_4$
Al-4Fe-0.1V	(minor, grey)	81 ± 0.06	14.58 ± 0.02	4.42 ± 0.01	19	-	V-doped Al_6Fe
Al-4Fe-0.5V	$\text{Al}_{13}\text{Fe}_4$ (minor, brighter)	75.23 ± 0.04	23.69 ± 0.02	1.08 ± 0.01	24.77	-	V-doped θ - $\text{Al}_{13}\text{Fe}_4$
Al-4Fe-0.5V	(major, grey)	81.49 ± 0.04	13.83 ± 0.02	4.68 ± 0.02	18.51	-	V-doped Al_6Fe
Al-4Fe-0.5V	(few, middle darker)	81.59 ± 0.05	13.2 ± 0.02	5.21 ± 0.02	18.41	-	V-doped Al_6Fe_2
Al-4Fe-0.5V	(few, most darker)	85.5 ± 0.04	5.95 ± 0.02	8.55 ± 0.02	14.5	-	Fe-doped Al_{23}V_4

Note: - in the table means non-detectable.

To understand the refinement mechanism of the Zr addition on the θ - $\text{Al}_{13}\text{Fe}_4$ particles (primary and eutectic), the Al-4Fe-0.5Zr alloy was solidified at a very slow cooling rate, 0.02 K/s. The examination results are shown in Figure 3. Figure 3a shows that the primary θ particles (grey) are more compact and exhibit fewer twins and branches when solidified at 0.02 K/s compared to those solidified at a higher cooling rate of 3.5 K/s. The primary zirconium-rich phase (brighter) exhibits a needle- or plate-like morphology when solidified at 0.02 K/s, which is distinct from the cubic morphology observed at the faster cooling rate of 3.5 K/s. Moreover, the number density of the primary Al_3Zr is much higher than that of the primary θ - $\text{Al}_{13}\text{Fe}_4$. It also demonstrates that there is at least one Al_3Zr particle is engulfed in the primary θ - $\text{Al}_{13}\text{Fe}_4$ particle. The further XRD investigation (Figure 3c) shows that the phases in the Al-4Fe-0.5Zr alloy solidified at 3.5 K/s are α -Al and θ - $\text{Al}_{13}\text{Fe}_4$ ($C2/m$ (12); monoclinic [31]) and Al_3Zr DO_{23} , respectively.

3.2. The Effects of V Addition on the Formation of θ - $\text{Al}_{13}\text{Fe}_4$

The effects of vanadium on the primary Fe-IMCs in Al-4Fe alloys with different amounts of vanadium solidified at 3.5 K/s were displayed in Figures 4 and 5. Each primary intermetallic compound was identified based on observed morphology, along with SEM-EDS and XRD analyses (Figure 6). The typical integrity ten-fold pure θ - $\text{Al}_{13}\text{Fe}_4$ phase was observed in Al-4Fe alloy, as shown in Figures 4a and 5a. The 3-dimensional (3D) morphology of θ - $\text{Al}_{13}\text{Fe}_4$ particles was presented in Figure 5b, showing a long needle and the ten-fold symmetry viewed along the cross section.

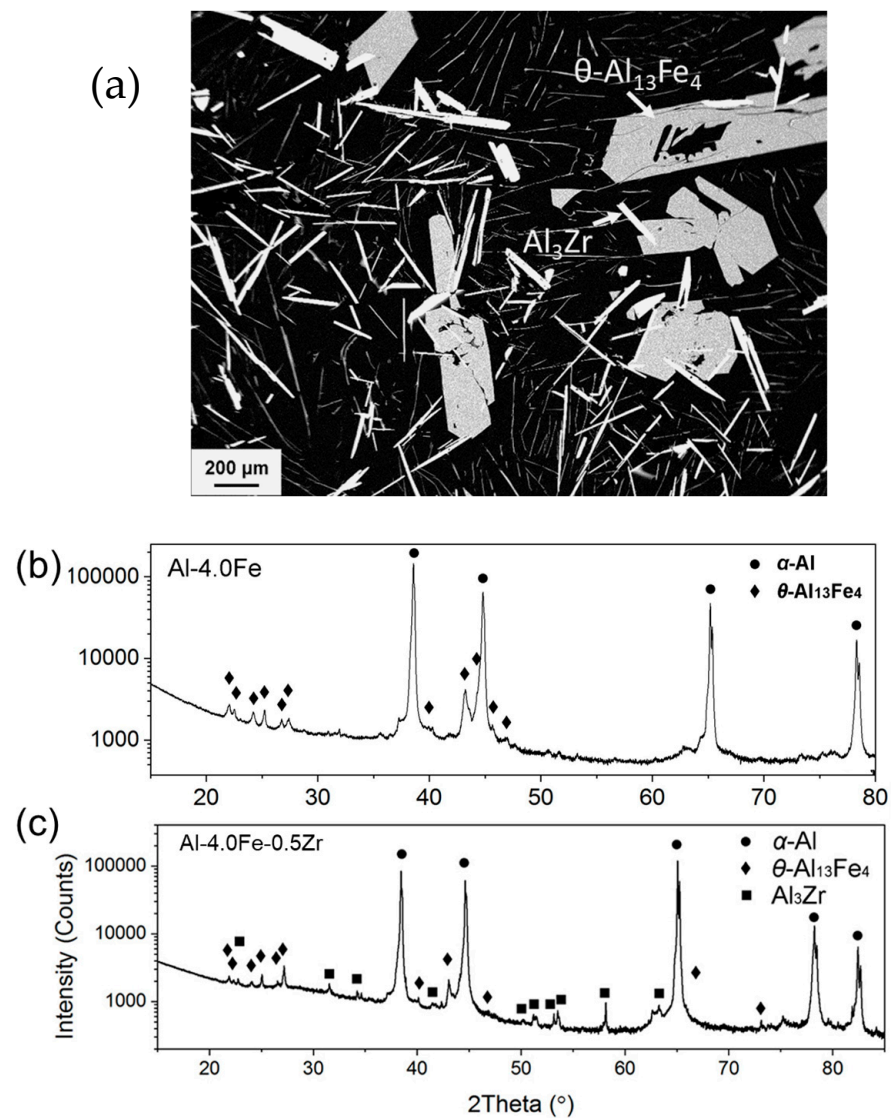


Figure 3. (a) The SEM image showing primary Al_3Zr (brighter) engulfed with the primary $\theta\text{-Al}_{13}\text{Fe}_4$ (grey) in Al-4Fe alloy-0.5Zr solidified at 0.02 K/s, and (b,c) the X-ray diffraction (XRD) identified the major phases in (b) Al-4Fe and (c) Al-4Fe-0.5Zr containing $\alpha\text{-Al}$, Al_3Zr and $\theta\text{-Al}_{13}\text{Fe}_4$.

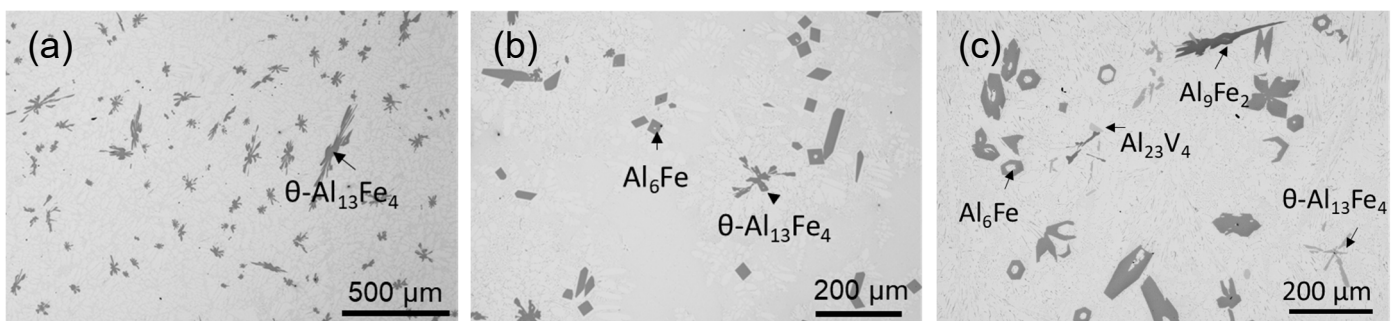


Figure 4. The OM images showing the morphology transition of the primary Fe-bearing intermetallic compounds (IMCs) in Al-4Fe alloys with different amounts of vanadium (V) solidified at 3.5 K/s. (a) 0% addition, (b) 0.1% addition of V with refined needed-like Fe-IMC, and (c) 0.5% addition of V with multiple types of Fe-IMCs with different morphologies.

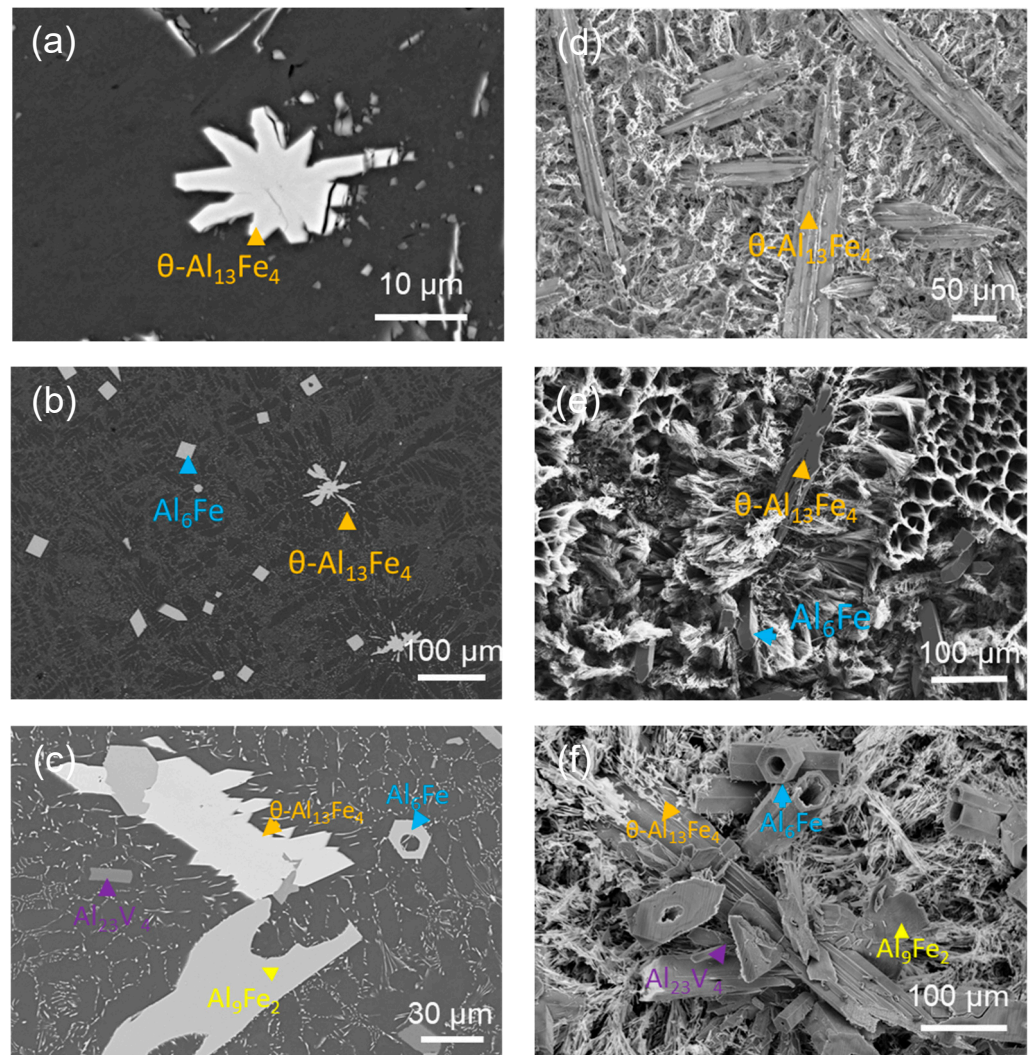


Figure 5. SEM-BSD images showing the morphology transition with different amounts of V in Al-4Fe alloys solidified at 3.5 K/s: (a) star-like (ten-folder) primary θ -Al₁₃Fe₄ (bright) in Al-4Fe alloy; (b) two types of intermetallic compounds including star-like primary θ -Al₁₃Fe₄ (bright) and some short hollowed needle-like compound Al₆Fe (grey) in Al-4Fe-0.1V alloy; (c) three types of IMCs including star-needle-like θ -phase (bright), short hollowed needle-like compound Al₆Fe (grey) and Al₉Fe₂ (grey), and Al₂₃V₄ (dark) compound in Al-4Fe-0.5V alloy, and 3D morphologies of IMCs shown in (a–c); (d) the needle-star-like θ -Al₁₃Fe₄ in Al-4Fe alloy; (e) the needle-star-like θ -Al₁₃Fe₄ and the short needle-like compound Al₆Fe in Al-4Fe-0.1V alloy; (f) mixed needle-star-like θ -Al₁₃Fe₄, the short needle-like compound Al₆Fe and plate-like Al₉Fe₂ and needle-like Al₂₃V₄ in Al-4Fe-0.5V alloy.

Figure 4b shows that, despite the minor addition of V (0.1%), the morphology of IMCs changed. Figures 4b and 5b,e demonstrate that in the Al-4Fe-0.1V alloy solidified at 3.5 K/s, a new type of primary IMCs with a needle-like morphology is formed, in contrast to the single star-like IMC shown in Figure 4a. The compound with star-like morphology was identified as pure θ -Al₁₃Fe₄ (Figure 4a), without incorporation with the other impurities in the Al-4Fe alloy. The SEM-EDS (Table 3) confirms that the compositions of these star-like IMC in the Al-4Fe-0.1V alloy are similar to those of the pure θ -phase, with a small amount V doping (~0.35 at.%). The average size of these star-like modified θ -phase particles was measured as $92.2 \pm 13.8 \mu\text{m}$. The number density was significantly reduced, with only a few modified θ -phase particles observed in this sample. It should be noted that the symmetry of the modified θ -Al₁₃Fe₄ particles in Al-4Fe-0.1V (Figure 5b) has been changed. It is difficult to observe the integrity of the ten-fold stars of θ -Al₁₃Fe₄. The majority of the

modified θ particles typically exhibit preferentially grown branches, although some have much shorter branches. The other type of intermetallic compound with hollowed needle-like instead of star-like morphology appears and becomes the dominated primary IMC. This type of IMC was identified as Al_6Fe with doping of V. The morphology of $\text{Al}_6\text{Fe}(\text{V})$ is similar to that of the $\text{Al}_6(\text{Fe},\text{Mn})$, which has a hollowed needle-like morphology [32]. These particles contain a significantly higher vanadium concentration (~ 4.42 at.%) compared to the modified θ -phase particles. However, Fe remains to be the major alloying element in these compounds. Figure 5e shows that the vanadium-modified Al_6Fe are shorter than the vanadium-modified $\theta\text{-Al}_{13}\text{Fe}_4$.

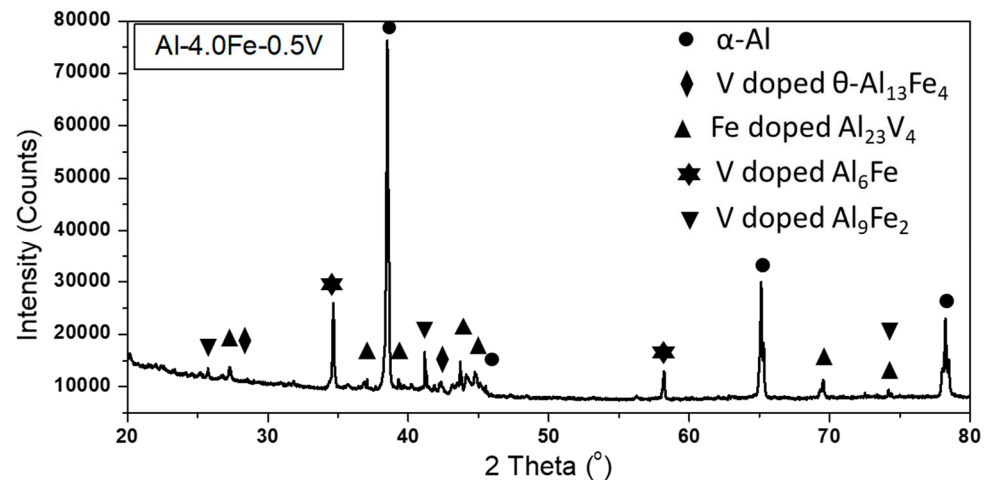


Figure 6. The XRD results identified four different types of IMCs in Al-4Fe-0.5V, which are Al_6Fe , Al_9Fe_2 , Al_{23}V_4 and $\theta\text{-Al}_{13}\text{Fe}_4$ followed by the sequence of the detected volume fraction from high to low.

Figures 4c and 5c,f reveal the as-cast microstructure of Al-4Fe-0.5V, which contains much more complex primary phase selection. Four types of intermetallic compounds with different morphologies can be observed as primary phases. A few star-like modified $\theta\text{-Al}_{13}\text{Fe}_4$ (long needles) with approximately 1.08 at.% vanadium doping, a majority of hollowed hexagonal Al_6Fe needles (shorter) with approximately 4.68 at.% vanadium doping, plate-like Al_9Fe_2 particles (large plates) with approximately 5.21 at.% vanadium doping and smaller needles of Al_{23}V_4 with approximately 5.95 at.% Fe doping can be observed.

The modified $\theta\text{-Al}_{13}\text{Fe}_4$ and Al_{23}V_4 can easily be defined from the microstructure due to their typical morphology (star-like θ) and brightness (darkest of Al_{23}V_4 under SEM). The modified Al_6Fe and Al_9Fe_2 have very similar brightness under SEM due to their very close compositions (Table 3). However, they have very different morphologies. Al_6Fe has the very typical hollowed hexagonal needle-like morphology, and the Al_9Fe_2 is less regular and more like the plate-like morphology (Figure 5c,f).

The XRD result from the Tp-1 sample of Al-4Fe-0.5V is displayed in Figure 6. Four different types of IMCs in this sample including Al_6Fe , Al_9Fe_2 , Al_{23}V_4 and $\theta\text{-Al}_{13}\text{Fe}_4$ were identified in order of the detected volume fraction, from high to low. Compared to the single compound ($\theta\text{-Al}_{13}\text{Fe}_4$) shown in Figure 3b, the phase selection in this alloy is much more complicated. It also shows that the volume fraction of $\theta\text{-Al}_{13}\text{Fe}_4$ decreased significantly compared to in the Al-4Fe alloy.

3.3. The Effects of Zr and V Addition on the Grain Refinement of $\alpha\text{-Al}$

The effects of the 0.5% Zr and 0.5% V addition on the grain refinement of Al-4Fe alloy are investigated and compared to that of the addition of the commercial Al-5Ti-1B grain refiner. The results are shown in Figure 7. The average grain size was measured and the results are listed in Table 2. They show that the addition of 0.5 wt.% Zr refined the $\alpha\text{-Al}$ grain size from $435.2 \pm 40.8 \mu\text{m}$ (without addition) to $63.1 \pm 2.8 \mu\text{m}$. However, the grain

size of Al-4Fe alloy with the addition of 0.5% Al-5Ti-1B grain refiner is only $153 \pm 3.1 \mu\text{m}$. Addition of 0.5% V did not refine the α -Al but refined the secondary dendritic arm spacing from $12.8 \pm 0.2 \mu\text{m}$ to $9.02 \pm 2.1 \mu\text{m}$.

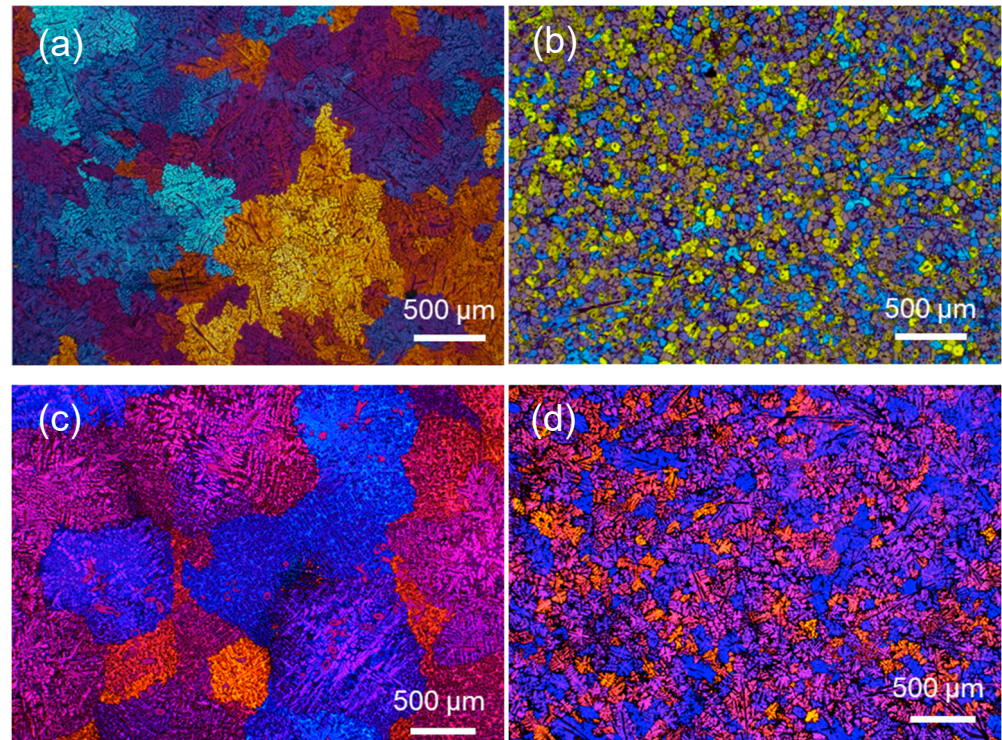


Figure 7. The optical microscope images of the anodized sample observed under the polarized light comparing the difference in grain refinement of α -Al in alloys solidified at 3.5 K/s: (a) Al-4Fe alloy, (b) Al-4Fe-0.5Zr, (c) Al-4Fe-0.5V and (d) Al-4Fe + 0.5 wt.% Al-5Ti-1B.

Further examination of the anodized samples of Al-4Fe and Al-4Fe-0.5Zr alloys solidified at 3.5 K/s is displayed in Figure 8. Figure 8a shows that the large-size primary θ - $\text{Al}_{13}\text{Fe}_4$ particles were engulfed within the α -Al grains. However, it is often observed that multiple primary θ - $\text{Al}_{13}\text{Fe}_4$ particles are found within a single α -Al grain, or that one θ - $\text{Al}_{13}\text{Fe}_4$ particle can span across several α -Al grains.

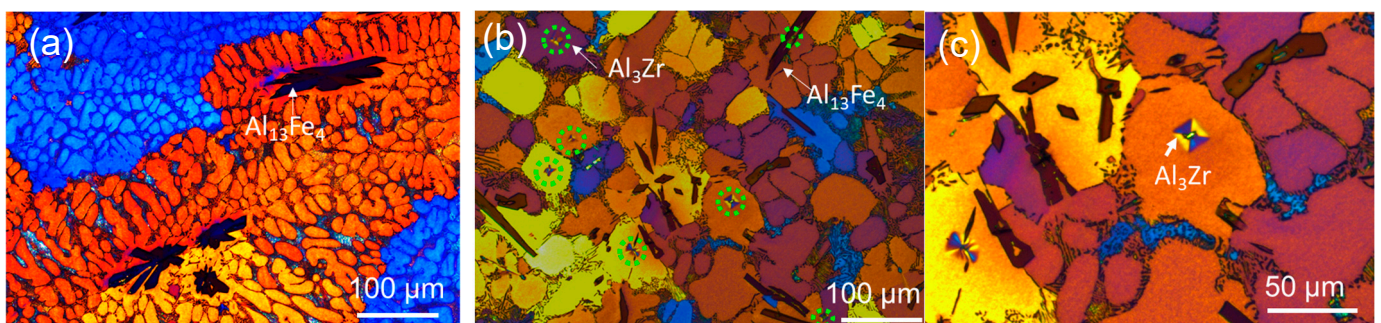


Figure 8. The optical microscope images of the anodized sample observed under the polarized light showing the engulfed particles in α -Al grains in alloys solidified at 3.5 K/s: (a) Al-4Fe alloy, (b) Al-4Fe-0.5Zr showing the Al_3Zr (in green dotted circles) sitting inside the α -Al rosettes, and (c) the high magnification image of (b) showing the centered Al_3Zr in α -Al grains.

Figure 8b shows that the cubic Al_3Zr particles in the Al-4Fe-0.5Zr alloys are frequently observed at the center of the α -Al grains. It shows that the Al_3Zr particles exhibit a square

morphology with four-fold symmetry after anodizing and are typically located within small α -Al rosettes. The majority of primary θ - $\text{Al}_{13}\text{Fe}_4$ particles extend across several α -Al rosettes. Only a few small-sized primary θ - $\text{Al}_{13}\text{Fe}_4$ particles can be observed that fully engulfed in one α -Al grain. The cubic Al_3Zr particles associated with the primary θ - $\text{Al}_{13}\text{Fe}_4$ particles can also be observed in Figure 8c.

The variation in the measured average sizes of θ - $\text{Al}_{13}\text{Fe}_4$ and α -Al in the Al-4Fe with different Zr additions is presented in Figure 9. It shows that the size of both θ - $\text{Al}_{13}\text{Fe}_4$ and α -Al decreased with the increasing addition of Zr. The refinement of both phases reaches a maximum with addition of 0.6 wt.% of Zr in the Al-4Fe alloy.

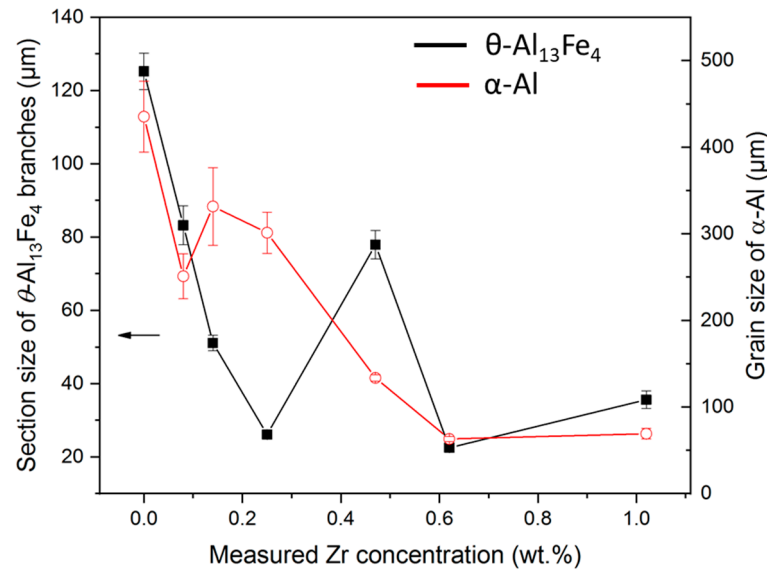


Figure 9. The variation in the measured size of θ - $\text{Al}_{13}\text{Fe}_4$ and α -Al with the addition of Zr in Al-4Fe alloy.

3.4. Formation Energies of V/Zr Solution in θ - $\text{Al}_{13}\text{Fe}_4$

To further investigate the doping capabilities of the alloying elements of Zr and V in the θ - $\text{Al}_{13}\text{Fe}_4$ crystal, the first-principle calculation was conducted. To have a measure of the relative stability of one M (=V or Zr) atom doped at one Fe or Al site in $\text{Al}_{13}\text{Fe}_4$ with respect to the parent intermetallic compound and the solute energy of V, Fe or Zr in the α -Al matrix, the formation energy per cell for impurity doping in the compounds is given by:

$$\Delta E_{dop}(\text{Al}_{13}(\text{Fe}_{1-x}\text{M}_x)_4) = E\{\text{Al}_{13}(\text{Fe}_{1-x}\text{M}_x)_4\} - \{E(\text{Al}_{13}\text{Fe}_4) + 4x[E(\text{M}) - E(\text{Fe})]\} \quad (1a)$$

$$\Delta E_{dop}((\text{Al}_{1-x}\text{M}_x)_{13}\text{Fe}_4) = E\{(\text{Al}_{1-x}\text{M}_x)_{13}\text{Fe}_4\} - \{E(\text{Al}_{13}\text{Fe}_4) + 13x[E(\text{M}) - E(\text{Al})]\} \quad (1b)$$

The unit of the formation energy is eV/cell. At the temperature $T = 0$ K and the pressure $p = 0$ Pa, the enthalpy difference is equal to the energy difference, $\Delta H = \Delta E$, when the zero-point vibration contribution is ignored.

A. V or Zr doping at the Fe sites in θ - $\text{Al}_{13}\text{Fe}_4$

The alloying elements doping into the θ - $\text{Al}_{13}\text{Fe}_4$ phase have two possibilities: solute at the Al sites or at the Fe sites. These two possibilities were carefully investigated, and the results are presented in Tables 4 and 5, respectively. Table 4 shows the calculated solute energies for V or Zr doping at the Fe sites in θ - $\text{Al}_{13}\text{Fe}_4$ with respect to the parental θ - $\text{Al}_{13}\text{Fe}_4$ and the V/Zr solute in the Al matrix, with ΔE_{dop} (eV/cell) according to Equation (1a). This shows that the formation energies for both V and Zr doping at the Fe sites in θ - $\text{Al}_{13}\text{Fe}_4$ (>1.3 eV) are high. The lowest energy costs for both V and Zr are the Fe5 sites (Wyckoff 8j sites) (Table 4). Doping a V atom at the Fe5 sites costs less than doping

a Zr atom at the same Fe site. The lowest energy cost is 1.33 eV for one V at Fe5, while it costs 3.04 eV for a Zr atom. Overall, the high energy costs associated with doping of V or Zr at the Fe site indicate suggest that such doping is unlikely to occur, even at the casting temperature (800 °C).

Table 4. Calculated solute energies for V or Zr doping at the Fe sites in θ -Al₁₃Fe₄ with respect to the parental θ -Al₁₃Fe₄ and the V/Zr solute in the Al matrix, ΔE_{dop} (eV/cell) according to Equation (1a). The unit of the formation energies is eV/unit-cell.

$\Delta E_{f1}/\Delta E_{f2}$	Fe1 Site, 4i	Fe2 Site, 4i	Fe3 Site, 4i	Fe4 Site, 4i	Fe5 Site, 8j
1 V	1.68	1.72	1.50	1.57	1.33
1 Zr	3.33	3.47	3.45	3.35	3.04

Table 5. Calculated solute energies for V or Zr doping at the 15 Al sites in θ -Al₁₃Fe₄ with respect to the parental θ -Al₁₃Fe₄ and the V/Zr solute in the Al matrix, ΔE_{dop} (eV/cell) according to Equation (1b). The unit of the formation energies is eV/unit-cell. The bold/italics numbers represent the lowest energy and the next to the lowest energy for the V/Zr doping at the Al sites, respectively.

Site, Wyckoff	$\Delta E_f(\text{V})$ eV/cell	$\Delta E_f(\text{Zr})$ eV/cell	Remarks
Al1, 4i	1.65	1.81	-Fe(\times 3)
Al2, 4i	2.13	1.37	-Fe(\times 2)
Al3, 4i	<i>0.60</i>	0.68	-Fe(\times 2)
Al4, 4i	0.76	1.72	-Fe(\times 4)
Al5, 4i	0.48	<i>0.81</i>	-Fe(\times 2)
Al6, 4i	1.59	2.10	-Fe(\times 3)
Al7, 2d	1.63	2.21	-Fe(\times 2)
Al8, 4i	0.76	1.55	-Fe(\times 3)
Al9, 4i	0.76	2.14	-Fe(\times 3)
Al10, 8j	1.36	1.75	-Fe(\times 3)
Al11, 8j	1.37	1.80	-Fe(\times 3)
Al12, 8j	1.23	1.48	-Fe(\times 3)
Al13, 8j	1.17	1.45	-Fe(\times 3)
Al14, 8j	1.34	1.99	-Fe(\times 2)
Al15, 4g	1.26	1.69	-Fe(\times 4)

B. V or Zr doping at the Al sites in θ -Al₁₃Fe₄

The solute energies for V or Zr doping at the 15 (Wyckoff) Al sites in θ -Al₁₃Fe₄ were calculated. The doping energy, ΔE_{dop} (eV/cell), is calculated according to Equation (1b). The results are shown in Table 5. It shows that the lowest energy cost is one Zr at the Al3 site and one V at Al5, respectively. In fact, doping a Zr or V at these two Al sites costs the lowest or second lowest energies as shown in Table 5. In θ -Al₁₃Fe₄, both Al3 and Al5 atoms have two Fe neighbors, indicating that both doped V and Zr atoms prefer less Fe neighbors. With respect to the binary θ -Al₁₃Fe₄ and elemental solid V, the formation energies range from 0.48 eV/cell to 2.13 eV for one V at an Al site, and 0.68 eV to 2.21 eV for one Zr at an Al site. Table 5 shows that energy cost to dope one V at the Al5 site is lower than that for one Zr at the Al3 sites. Doping both vanadium and zirconium at the Al sites incurs significantly lower energy costs compared to doping at the Fe sites. Although the doping energy of vanadium in the Al5 sites is relatively low, it remains positive, indicating that doping is challenging under ambient conditions, as the first-principle calculations

were performed at 0 K. To better understand the experimental results, the thermodynamic analysis is carried based on the above first-principle calculation.

C. Thermodynamic Analysis

The formation temperature of primary θ -Al₁₃Fe₄ in the Al-4Fe alloy was calculated to be 745 °C using the Scheil model. It is reported that the nucleation of Fe-IMCs is difficult and requires large nucleation undercooling [13]. The nucleation undercooling of θ -Al₁₃Fe₄ is approximately ~10 K [33]. Therefore, the thermodynamic calculation in this section will be taken at 1000 K (737 °C). Configuration entropy contribution enables a certain content of impurities into the lowest energy-cost sites, e.g., V at the Al5 and Zr at the Al3 sites. Here, we estimate the amounts of V/Zr impurities at the related sites according to the Gibbs energy (ΔG) relation:

$$\Delta G = \Delta H - T \Delta S \quad (2)$$

Here, ΔH is the reaction enthalpy, T the temperature and $\Delta S = R \ln W$ is the configurational entropy with R being the Boltzmann constant, the W the number of configurations of the same formation enthalpy. Thus, we may get $W = \exp(\Delta H/RT)$ with $\Delta G = 0$.

For one V at the Al5 (4i) sites, $\Delta H = \Delta E = 0.475$ eV, which gives $W = 248$ at 1000 K. Using a random distribution model for one V at the Al5 (4i) sites, we obtained V concentration $x = 0.12\%$ in the formula θ -(Al_{1-x}V_x)₁₃Fe₄. In other words, there are approximately 0.1% of Al atoms can be doped by V in θ -(Al_{1-x}V_x)₁₃Fe₄.

Using the same equation for Zr doping at the Al3 sites with $\Delta H = 0.676$ eV gives $W = 2552$. Correspondingly, we obtain $x = 0.012\%$ in the formula θ -(Al_{1-x}Zr_x)₁₃Fe₄, which is approximately one order of magnitude less than the V doping. This result indicates limited possibilities for V doping in θ -Al₁₃Fe₄ based, but almost no possibility for Zr doping in θ -Al₁₃Fe₄.

4. Discussion

4.1. Composition, Structure and Morphology Variation in θ -Al₁₃Fe₄ Caused by Zr and V

The current experimental results demonstrated that zirconium cannot be incorporated into θ -Al₁₃Fe₄, and Fe cannot be incorporated into Al₃Zr, even in the Al-4Fe alloy with addition of Zr up to 0.5 wt.%. First-principle calculation also indicated high energy costs for Zr doping at both the Fe sites and the Al sites in θ -Al₁₃Fe₄. θ -Al₁₃Fe₄ has the monoclinic crystal structure with space group, C 1 2/m. For the pure θ -Al₁₃Fe₄ particles, it is common to observe the ten-fold branches, as shown in Figure 5a, when solidified at a fast cooling rate, e.g., 3.5 K/s. However, when solidified at slow cooling rate such as 0.02 K/s, it is less likely to see the ten-fold twinning branches.

Further, the addition of different compositions can affect the morphology of θ -Al₁₃Fe₄, resulting in a reduced number of branches, particularly the twinning branches. A previous study [34] reported that in the Al-4Fe-4Si alloy, only up to six-fold twinning branches can be observed in θ -Al₁₃Fe₄ particles with Si incorporation. In this study, with the addition of 0.5 wt.% Zr, some small primary θ -Al₁₃Fe₄ particles exhibited no branches at all, as these particles did not have enough time to grow.

Our experimental observations revealed that vanadium can be incorporated into θ -Al₁₃Fe₄, slightly modifying its morphology in the Al-4Fe alloy, even with minor addition of vanadium (0.1 wt.%). In return, Fe can also be incorporated into V compounds (Table 3). The addition of varying vanadium content significantly reduced the volume fraction of the primary θ -Al₁₃Fe₄ phase (Figure 4), leading to the formation of other iron-rich and vanadium-rich compounds that became the dominant primary intermetallic compounds in Al-4Fe alloys. The introduction of a small amount of vanadium doping in the θ -Al₁₃Fe₄ phase resulted in the suppression of certain twinning branches (Figure 5b). This phenomenon may be linked to the occupation of atomic positions by vanadium within the θ -Al₁₃Fe₄ crystal structure.

The mechanisms behind the differing experimental results of 3d and 4d transition metal doping (specifically Zr and V) in θ -Al₁₃Fe₄ have been investigated using first-principle

calculations (Tables 4 and 5). It has been demonstrated that doping V or Zr at the Fe sites in θ - $\text{Al}_{13}\text{Fe}_4$ incurs a high energy cost. The first-principle study also revealed that doping V at one of the Wyckoff Al 4i sites costs approximately 0.48 eV (at 0 K), which is notably lower than the energy cost associated with doping V at the Fe sites. Such a low energy cost suggests that a minor amount of V (approximately 0.1 at.%) can be effectively doped into θ - $\text{Al}_{13}\text{Fe}_4$ at the casting temperature (800 °C). The phase diagram calculation in Figure 10 showed that the AlV phases are the more stable primary phase compared to θ - $\text{Al}_{13}\text{Fe}_4$. The phase diagram of Al-4Fe-xV alloys and the solidification curve of Al-4Fe-0.5V alloy were calculated and shown in Figure 10a and Figure 10b, respectively. A solidification sequence as: θ - Al_{13}M_4 , (θ + Al_3V), (θ + Al_{23}V_4), (Al_{23}V_4 + Al_7V), and (Al_{13}M_4 + α -Al) was predicted. The doping of V in various types of Fe-IMCs might change the nucleation potency and the difficulties associated with nucleation. Therefore, during the non-equilibrium casting process in this study, multiple types of Fe-IMCs such as θ - $\text{Al}_{13}\text{Fe}_4$, Al_6Fe and Al_9Fe_2 , can be co-selected at different solidification stages before the α -Al is solidified. Once the Fe-based intermetallic compounds (IMCs) are solidified, the consumption of vanadium (V) in these compounds altered the concentration of V in the melt. This change subsequently affected the formation behavior of the vanadium-based intermetallic compounds (V-IMCs). Therefore, only one type of V-IMC (Al_{23}V_4) was solidified in Al-4Fe-0.5V in this study.

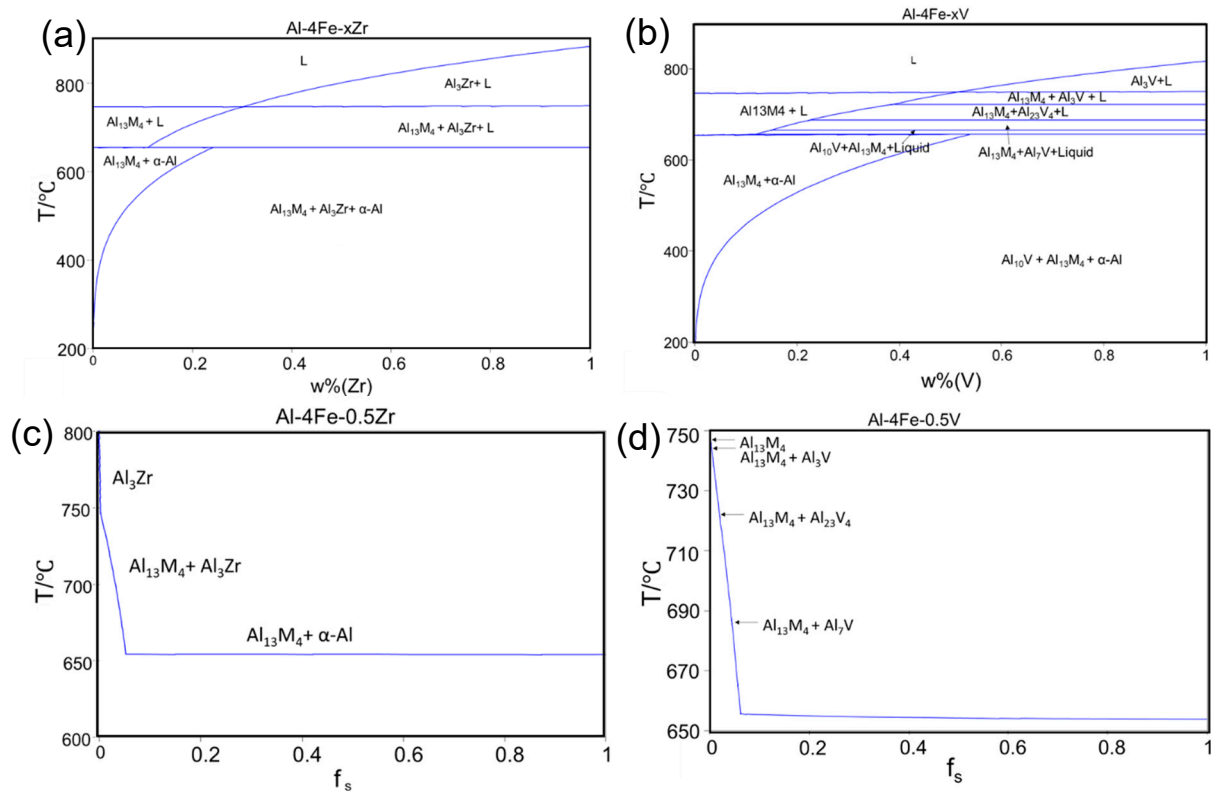


Figure 10. The calculated phase diagram and solidification curves of Al-4Fe-X alloys, (a) Al-4Fe-xZr, (b) Al-4Fe-xV, (c) Al-4Fe-0.5Zr and (d) Al-4Fe-0.5V.

However, the formation of the primary phases is dependent on multiple factors such as alloy compositions, heterogeneous nucleation and the phase stability. Therefore, the phase competition among various primary IMCs, including θ - $\text{Al}_{13}\text{Fe}_4$, Al_6Fe , Al_9Fe_2 , Al_{23}V_4 in the studied Al-4Fe-xV, can be explained. This mechanism can also be applied to explain the formation of the mixed primary θ - $\text{Al}_{13}\text{Fe}_4$, Zr-rich compounds in Al-4Fe-0.5Zr alloys.

The general understanding is that doping 3d transition metals, such as Cr, Mn, Co, Ni, into Al_{13}M_4 phase involves replacing Fe atoms [16,17]. This study reveals for the first time that certain 3d transition metals, such as vanadium (V), can dope into the Al_{13}M_4

phase by replacing aluminum (Al) atoms at a specific site (Al5). This may be attributed to difference in electronic configurations: V, being an early transition metal, contains three 3d electrons (the electronic configuration [Ar] 3d³ 4s²), which is much lower than that of the later 3d transition metal Fe, which contains six 3d electrons with the electronic configuration [Ar] 3d⁶ 4s². Previous investigations showed that the early transition metals, such as Sc, Ti, V, as well as the 4d element Zr prefer for forming Al₃T-type phases, the structures of which exhibit face-centered cubic-based coordination [35]. Meanwhile the later 3d transition metals, such as Fe, Ni, and Co, react with Al to form more complex structures, such as θ -Al₁₃M₄ type, which exhibit a rich variety of local coordination [36,37]. The large differences in the number of d-electrons cause high energy costs to replace Fe by V in the θ -Al₁₃Fe₄ structure. Similarly, the early transition 4d element Zr has a much different electronic configuration ([Kr] 4d² 5s²), which means high energy costs for Zr to replace iron in the complex θ -Al₁₃Fe₄ structure).

4.2. Mechanism of the Refinement of α -Al and θ -Al₁₃Fe₄ by Addition of 0.5 wt.% Zr

The as-cast microstructure shown in Figures 1 and 7 demonstrated that the addition of 0.5 wt.% Zr to the Al-4Fe alloy not only significantly refined the primary θ -Al₁₃Fe₄, but also greatly reduced the size of the α -Al grains. According to current understandings on the heterogeneous nucleation, all the of solid surfaces, including the casting mold in contact with the alloy melt, can serve as nucleation substrates with varying degrees of potency. The potential solid particles in the melt before the solidification of α -Al include pre-existing inclusions such as oxides, carbides, and nitrides, as well as newly solidified Al₃Zr, other types of non-equilibrium primary Zr-rich IMCs and primary θ -Al₁₃Fe₄.

The phase diagram calculation shown in Figure 10a and Figure 10c indicates that the Al₃Zr will be solidified in advance of θ -Al₁₃Fe₄. The solidification sequence of Al-4Fe-0.5Zr alloy is: Al₃Zr, (Al₃Zr+ θ -Al₁₃Fe₄), and (θ -Al₁₃Fe₄ + α -Al). It is reported [38] that in the Mg-free aluminum alloys, native inclusions such as Al₂O₃ and AlN have been examined. These particles could serve as the potential nucleation substrate for Al₃Zr compounds. Thereafter, the potential nucleation substrates for primary θ -Al₁₃Fe₄ could be the native inclusions and the Al-Zr compounds.

In this study, the experimental results clearly demonstrated that the addition of 0.5 wt.% Zr in Al-4Fe alloy significantly refined the primary θ -Al₁₃Fe₄ and increased its number density. Therefore, there are two possible mechanisms for the refinement of θ -Al₁₃Fe₄ resulting from the addition of Zr in the Al-4Fe alloy. One possibility is that the nucleation potency of native inclusions, such as Al₂O₃ particles, was enhanced from being ineffective for the nucleation of θ -Al₁₃Fe₄ due to the interfacial segregation of Zr. It is reported that the interfacial conditions such as structural templating or composition templating of nucleation substrates can be modified by the constitute alloy elements [39]. Therefore, the nucleation potency of the substrates could be changed from impotent to potent, such as the 2-dimensional compound Al₃Ti formation on (0 0 0 1) surface of TiB₂ particles in Al-5Ti-1B master alloy, which reduced the misfit between Al/TiB₂ from 4.2% to 0.09% [39]. The other possibility is that primary Al-Zr particles, which formed earlier at higher temperature, acted as nucleation substrates for the θ -Al₁₃Fe₄. Further experimental results indicated that the Al-Zr compounds associated with θ -Al₁₃Fe₄ support the second possibility.

Before the formation of the α -Al grains, the solid particles in the melt included various pre-existing inclusions, as well as the solidified Zr-rich IMCs and θ -Al₁₃Fe₄. Due to the size effects on the heterogeneous nucleation [40], larger particles have a higher potency for promoting grain refinement. Therefore, the solidified Zr-rich IMCs and θ -Al₁₃Fe₄ have a greater chance of nucleating the following α -Al. Thus, the competition between these two types of large particles for the grain refinement of α -Al grains will be discussed here. The experimental results (Figures 7 and 8) demonstrated that the majority of α -Al grains were observed to contain Al₃Zr particles. Some primary θ -Al₁₃Fe₄ were observed to be engulfed within a few α -Al grains, while the majority were found lying across several α -Al

grains. Although the possibility of the α -Al nucleated heterogeneously on the θ -Al₁₃Fe₄ cannot be excluded, the grain refinement of the α -Al grains is primarily attributed to the Al₃Zr particles formed in the Al-4Fe-0.5Zr alloy.

5. Conclusions

- (1) Zirconium cannot be doped into θ -Al₁₃Fe₄, nor can Fe be incorporated into Al₃Zr, in the Al-4Fe alloy with up to 0.5 wt.% addition of Zr in this study. In contrast, vanadium can be doped into θ -Al₁₃Fe₄, slightly modifying its morphology with a minor addition of 0.1 wt.%V. As the concentration of V increases, θ -Al₁₃Fe₄ becomes unstable, leading to the formation of other types of Al-Fe-V phases.
- (2) With an addition of 0.5 wt.% Zr, the average size of θ -Al₁₃Fe₄ in Al-4Fe alloys was refined from $120.3 \pm 13.2 \mu\text{m}$ to $22.5 \pm 0.9 \mu\text{m}$, while the number density of θ -Al₁₃Fe₄ in Al-4Fe alloys was increased from $39.5 \pm 2.4 \text{mm}^{-2}$ to $194.4 \pm 32.5 \text{mm}^{-2}$.
- (3) With an addition of 0.5 wt.% Zr, the grain size of α -Al in Al-4Fe alloys was reduced from $435.2 \pm 40.8 \mu\text{m}$ to $63.1 \pm 2.8 \mu\text{m}$.
- (4) The cuboidal Al₃Zr phase, which is engulfed within the α -Al grain, contributes to the grain refinement of both α -Al and θ -Al₁₃Fe₄.
- (5) The binary eutectic θ -Al₁₃Fe₄ + α -Al was refined in the Al-4Fe-0.5Zr alloy due to a modified solidification sequence.
- (6) The lowest formation energy for V doping in θ -Al₁₃Fe₄ occurs when it occupies the Al₅ sites, rather than any Fe site. In contrast, the formation energies of Zr occupying both the Al and Fe sites are relatively high when doping into θ -Al₁₃Fe₄.

Author Contributions: Z.Q., conceptualization, experiments, methodology, writing, editing and reviewing. C.F., first-principle calculation and reviewing. J.X., experiments. Z.F., funding. All authors have read and agreed to the published version of this manuscript.

Funding: This research was funded by the Engineering and Physical Sciences Research Council (EPSRC) is gratefully acknowledged for providing financial support under Grant EP/N007638/1 for LiME hub and the Brunel University London BRIEF award (11937131).

Data Availability Statement: The original contributions presented in this study are included in this article, and further inquiries can be directed to the corresponding author.

Acknowledgments: Thanks go to our colleague Chamini L. Mendis for XRD technique support.

Conflicts of Interest: The authors declare no conflicts of interest.

References

1. Que, Z.; Wang, Y.; Mendis, C.L.; Fang, C.; Xia, J.; Zhou, X.; Fan, Z. Understanding Fe-containing intermetallic compounds in Al alloys: An overview of recent advances from the LiME research hub. *Metals* **2022**, *12*, 1677. [[CrossRef](#)]
2. Khalifa, W.; Samuel, A.M.; Samuel, F.H.; Doty, H.W.; Valtierra, S. Metallographic observations of β -AlFeSi phase and its role in porosity formation in Al-7%Si alloys. *Int. J. Cast Met. Res.* **2006**, *19*, 156–166. [[CrossRef](#)]
3. Mbuya, T.O.; Odera, B.O.; Ng'ang'a, S.P. Influence of iron on castability and properties of aluminium silicon alloys: Literature review. *Int. J. Cast Met. Res.* **2003**, *16*, 451–465. [[CrossRef](#)]
4. Samuel, E.; Samuel, A.M.; Doty, H.W.; Valtierra, S.; Samuel, F.H. Intermetallic phases in Al-Si based cast alloys: New perspective. *Int. J. Cast Met. Res.* **2014**, *27*, 107–114. [[CrossRef](#)]
5. Lu, L.; Dahle, A.K. Iron-rich intermetallic phases and their role in casting defect formation in hypoeutectic Al-Si alloys. *Metal. Mater. Trans. A* **2005**, *36A*, 819–835.
6. Zhang, L.; Gao, J.; Damoah, L.N.W.; Robertson, D.G. Removal of iron from Aluminum: A Review. *Miner. Process. Extr. Metall. Rev.* **2012**, *33*, 99–157. [[CrossRef](#)]
7. Lazaro-Nebreda, J.; Patel, J.B.; Chang, I.T.H.; Stone, I.C.; Fan, Z. Solidification processing of scrap Al-alloys containing high levels of Fe. *IOP Conf. Ser. Mater. Sci. Eng.* **2019**, *529*, 012059. [[CrossRef](#)]
8. Osawa, Y.; Takamori, S.; Kimura, T.; Minagawa, K.; Kakisawa, H. Morphology of intermetallic compounds in Al-Si-Fe alloy and its control by ultrasonic vibration. *Mater. Trans.* **2007**, *48*, 2467–2475. [[CrossRef](#)]
9. Cao, X.; Campbell, J. Effect of melt superheating on convection-free precipitation and sedimentation of primary α -Fe phase in liquid Al-11.5 Si-0.4 Mg alloy. *Int. J. Cast Met. Res.* **2003**, *15*, 595–608. [[CrossRef](#)]

10. Ahmad, R.; Marshall, R.I. Effect of superheating on iron-rich plate-type compounds in aluminium-silicon alloys. *Int. J. Cast Met. Res.* **2003**, *15*, 497–504. [CrossRef]
11. Song, X.; Gao, M.; Yang, B.; Guan, R. Modification and refinement of Fe-containing phases, mechanical properties and strengthening mechanisms in Al–Fe alloys via Cr alloying and continuous rheo-extrusion. *Mater. Sci. Eng. A* **2022**, *850*, 143557. [CrossRef]
12. Lin, S.; Dang, J.; Wang, Z.; Sun, Y.; Xiang, Y. Enhanced Strength and Toughness in Al–Mg–Si Alloys with Addition of Cr, Mn, and Cu Elements. *J. Mater. Eng. Perform.* **2023**, *32*, 1039–1050. [CrossRef]
13. Que, Z.; Wang, Y.; Fan, Z.; Hashimoto, T.; Zhou, X.R. Composition templating for heterogeneous nucleation of intermetallic compounds. *Sci. Rep.* **2024**, *14*, 8968. [CrossRef] [PubMed]
14. Pang, N.; Shi, Z.M.; Wang, C.Q.; Li, N.Y.; Lin, Y.M. Influence of Cr, Mn, Co and Ni addition on crystallization behaviour of Al₁₃Fe₄ phase in Al–5Fe alloys based on thermodynamic calculations. *Materials* **2021**, *14*, 768. [CrossRef]
15. Lafaye, P.; Oishi, K.; Bourdon, M.; Harvey, J.-P. Crystal Chemistry and thermodynamic modelling of Al₁₃(Fe,TM)₄ solid solutions (TM = Co, Cr, Ni, Pt). *J. Alloys Compd.* **2022**, *920*, 165779. [CrossRef]
16. Liu, C.; Fan, C.Z. Crystal structure of the λ-Al₁₃Fe₄-type intermetallic (Al,Cu)₁₃(Fe,Cu)₄. *IUCrData* **2018**, *3*, 180363. [CrossRef]
17. Mahran, M.A.G.; Omran, A.-N.M. Grain refining of aluminium 6063 alloys using Al–V alloy containing Al₃V intermetallic compound. *Mater. Sci.* **2022**, *28*, 41–47. [CrossRef]
18. Wang, F.; Qiu, D.; Liu, Z.-L.; Taylor, J.A.; Easton, M.A.; Zhang, M.-X. The grain refinement mechanism of cast aluminium by zirconium. *Acta Mater.* **2013**, *61*, 5636–5645. [CrossRef]
19. Chankitmongkong, S.; Eskin, D.G.; Limmaneevichitr, C. Structure refinement, mechanical properties and feasibility of deformation of hypereutectic Al–Fe–Zr and Al–Ni–Zr alloys subjected to ultrasonic melt processing. *Mater. Sci. Eng. A* **2020**, *788*, 139567. [CrossRef]
20. Pazuon, C.; Buttard, M.; Despres, A.; Chehab, B.; Blandin, J.-J.; Martin, G. A novel laser powder bed fusion Al–Fe–Zr alloy for superior strength-conductivity trade-off. *Scr. Mater.* **2022**, *219*, 114878. [CrossRef]
21. Morozova, A.; Mogucheva, A.; Bukin, D.; Lukianova, O.; Korotkova, N.; Belov, N.; Kaibyshev, R. Effect of Si and Zr on the Microstructure and Properties of Al–Fe–Si–Zr Alloys. *Metals* **2017**, *7*, 495. [CrossRef]
22. Ye, J.; Guan, R.; Zhao, H.; He, C.; Xiong, K. Effect of Zr microalloying on the microstructures and strengthening mechanism of as-cast Al–Fe–Zr alloys. *Materials* **2020**, *13*, 4744. [CrossRef] [PubMed]
23. *Standard Test Procedure for Aluminum Alloy Grain Refiners: TP-1*; The Aluminum Association: Washington, DC, USA, 1987; p. 22.
24. Available online: <https://compuharm.com/panaluminum> (accessed on 1 January 2021).
25. Scheil, E.Z. Bemerkungen zur Schichtkristallbildung. *Z. Metallkd.* **1942**, *34*, 70–72. [CrossRef]
26. Kresse, G.; Hafner, J. Ab initio molecular-dynamics simulation of the liquid-metal-amorphous-semiconductor transition in germanium. *Phys. Rev. B* **1994**, *49*, 14251–14269. [CrossRef]
27. Blöchl, P.E. Projector augmented-wave method. *Phys. Rev. B* **1994**, *50*, 17953–17978. [CrossRef]
28. Perdew, J.P.; Burke, K.; Ernzerhof, M. Generalized gradient approximation made simple. *Phys. Rev. Lett.* **1996**, *77*, 3865–3868. [CrossRef]
29. Fang, C.M.; Sluiter, M.H.F.; van Huis, M.A.; Ande, C.K.; Zandbergen, H.W. Origin of predominance of cementite among iron carbides in steel at elevated temperature. *Phys. Rev. Lett.* **2010**, *105*, 055503. [CrossRef] [PubMed]
30. Monkhorst, H.J.; Pack, J.D. Special points for Brillouin-zone integrations. *Phys. Rev. B* **1976**, *13*, 5188–5192. [CrossRef]
31. Grin, J.; Burkhardt, U.; Ellner, M.; Peters, K. Refinement of the Fe₄Al₁₃ structure and its relationship to the quasihomological homeotypical structures. *Z. Krist.-Cryst. Mater.* **1994**, *209*, 479–487. [CrossRef]
32. Que, Z.; Wang, Y.; Fan, Z.; Hashimoto, T.; Zhou, X. Enhanced heterogeneous nucleation of Al₆(Fe, Mn) compound in Al alloys by interfacial segregation of Mn on TiB₂ particles surface. *Mater. Lett.* **2022**, *323*, 132570. [CrossRef]
33. Que, Z.; Zhou, Y.; Wang, Y.; Fan, Z. Composition templating for heterogeneous nucleation of intermetallic compounds. In Proceedings of the 6th Decennial International Conference on Solidification, Windsor, UK, 25–27 July 2017; pp. 1–5.
34. Que, Z.; Mendis, C.L. Effects of Si solution in θ-Al₁₃Fe₄ on phase transformation between Fe-containing intermetallic compounds in Al alloys. *J. Alloys Compd.* **2023**, *932*, 167587. [CrossRef]
35. Khan, A.V.; Eskin, D.G.; Starodub, K.F.; Dinsdale, A.T.; Wang, F.; Fang, C.M.; Cheverrikin, V.V.; Gorshenkov, M.V. New insights into solidification and phase equilibria in the Al–Al₃Zr system: Theoretical and experimental investigations. *J. Alloys Compd.* **2018**, *743*, 626–638.
36. Saito, K.; Sugiyama, K.; Hiraga, K. Al₁₃M₄-type structures and atomic models of their twins. *Mater. Sci. Eng. A* **2000**, *294–296*, 279–282. [CrossRef]
37. Jeglič, P.; Vrtnik, S.; Bobnar, M.; Klanjšek, M.; Bauer, B.; Gille, P.; Grin, Y.; Haarmann, F.; Dolinšek, J. M–Al–M groups trapped in cages of Al₁₃M₄ (M = Co, Fe, Ni, Ru) complex intermetallic phases as seen via NMR. *Phys. Rev. B* **2010**, *82*, 104201. [CrossRef]
38. Que, Z.; Mendis, C.L. Effects of native AlN particles on heterogeneous nucleation in an Al–3Fe Alloy. *Metall. Mater. Trans. A* **2021**, *52*, 553–559. [CrossRef]

39. Fan, Z.; Wang, Y.; Zhang, Y.; Qin, T.; Zhou, X.R.; Thompson, G.E.; Pennycook, T.; Hashimoto, T. Grain refining mechanism in the Al/Al–Ti–B system. *Acta Mater.* **2015**, *84*, 292–304. [[CrossRef](#)]
40. Greer, A.L.; Bunn, A.M.; Tronche, A.; Evans, P.V.; Bristow, D.J. Modelling of inoculation of metallic melts: Application to grain refinement of aluminium by Al–Ti–B. *Acta Mater.* **2000**, *48*, 2823–2835. [[CrossRef](#)]

Disclaimer/Publisher’s Note: The statements, opinions and data contained in all publications are solely those of the individual author(s) and contributor(s) and not of MDPI and/or the editor(s). MDPI and/or the editor(s) disclaim responsibility for any injury to people or property resulting from any ideas, methods, instructions or products referred to in the content.